The GALAH Survey: Verifying abundance trends in the open cluster M67 using non-LTE spectroscopy

X. D. Gao[1]★, K. Lind[1,2], A. M. Amarsi[1], et al.
[1]Max Planck Institute für Astronomy, Königstuhl 17, D-69117 Heidelberg, Germany
[2]Department of Physics and Astronomy, Uppsala University, Box 516, SE-751 20 Uppsala, Sweden

Accepted —. Received —; in original form —

ABSTRACT

Open cluster members are coeval and share the same initial bulk chemical compositions. Consequently, differences in surface abundances with stellar evolutionary stage can be used to study the effects of mixing and internal chemical processing. We carry out an abundance analysis of seven elements (Li, O, Na, Mg, Al, Si, Fe) in 69 stars belonging to the open cluster M67, based on high resolution GALAH spectra, 1D MARCS model atmospheres, and, for the first time for a large sample of M67 stars, non-local thermodynamic equilibrium (non-LTE) radiative transfer. From the non-LTE analysis, we find a typical star-to-star scatter in the abundance ratios of around 0.05 dex; this scatter is slightly but systematically larger when LTE is assumed instead. We find trends in the abundance ratios with effective temperature, indicating systematic differences in the surface abundances between dwarf and giant stars; these trends are more pronounced when LTE is assumed, however, in the non-LTE analysis, most of the element trends has been flattened, except for Al and Si for which they still have clearly remaining trends. We comment on the possible origin of these trends, by comparing them against recent stellar models that include atomic diffusion.

Key words: radiative transfer — Stars: atmospheres — Stars: abundances — Stars: late-type — Open clusters: individual (M67)

1 INTRODUCTION

Under the assumption that open clusters have undergone a single burst of star formation from a chemically homogeneous and well-mixed progenitor cloud (e.g. De Silva et al. 2006; Randich et al. 2006; De Silva et al. 2007; Pancino et al. 2010; Magrini et al. 2014), open cluster members are coeval, and share the same initial bulk chemical compositions, differing only in their initial stellar masses. Based on the chemical homogeneity in star clusters, chemical tagging proposed by Freeman & Bland-Hawthorn (2002) can be used to reconstruct stellar groups that have been dispersed. For example, Kos et al. (2018) have successfully identified two new members of the Pleiades, located far from the cluster centre, with chemical tagging and recovered seven observed clusters in chemical space by using t-distributed stochastic neighbour embedding (t-SNE). To support chemical tagging in Galactic Archaeology, a large amount of high quality observed data will be provided by massive high resolution spectroscopic surveys such as GALAH (De Silva et al. 2015), 4MOST (de Jong et al. 2012), Gaia-ESO (Gilmore et al. 2012) and APOGEE (Majewski et al. 2017).

However, recent studies have demonstrated that, in the same open cluster, the surface abundances measured in (unevolved) dwarf stars are apparently offset compared to those measured in (evolved) giant stars (e.g. Villanova et al. 2009; Schuler et al. 2009; Önehag et al. 2014; Martin et al. 2017). These trends with evolutionary stage cannot be explained by the standard model of stellar evolution, in which convection is the only internal mixing process.

Atomic diffusion is one possible explanation for these surface abundance trends (Michaud et al. 1984). Atomic diffusion can perturb the surface abundances of late-type dwarfs with shallow convection zones: different chemical species will be underabundant or overabundant to varying degrees in the stellar atmosphere, depending on the competing effects of gravitational settling and radiative acceleration. Furthermore, once the star leaves the turn-off point and starts climbing the red giant branch, the deeper convection zone will restore the original composition in the atmosphere.

Systematic abundance trends with evolutionary stage have also been measured in a number of globular clusters, which can be well described by using atomic diffusion models with extra turbulent mixing below the convection zone. (e.g. Korn et al. 2007; Lind et al. 2009b; Nordlander et al. 2012; Gruyters et al. 2014, 2016). However, these globular clusters are old and only probe the low metallicity regime ($-2.3 < [Fe/H] < -1.5$). They also show anti-correlations in some light elements, which is thought to be produced by intra-cluster pollution by short-lived stars of the first cluster generation (e.g. Prantzos & Charbonnel 2006). In contrast, open

★ E-mail:gao@mpia.de

clusters probe the metallicity and age range typical of the Galactic disk, and have not experienced such internal pollution. Thus, the stellar surface compositions of open cluster members should truly reflect the primordial abundances from the proto-cluster, unless they have been altered by evolutionary effects. Open clusters are thus better candidates for putting observational constraints on atomic diffusion models.

M67 is an ideal target to study such phenomena. Its proximity to us (Sarajedini et al. 2009; Yakut et al. 2009) permits a detailed spectroscopic study of even its main-sequence stars. M67 has been widely studied, and different studies has obtained slight different results, with different authors claiming different averaged metallicities between −0.04 to +0.05 (Hobbs & Thorburn 1991; Tautvaišiene et al. 2000; Yong et al. 2005; Randich et al. 2006; Pasquini et al. 2008; Pace et al. 2008), and different ages between 3.5 to 4.8 Gyr (Yadav et al. 2008; Önehag et al. 2011). Considering the uncertainties in different studies, they all draw the same conclusion: that the chemical composition and age of M67 are similar to the Sun. It has even been suggested that this is the original birthplace of the Sun (Önehag et al. 2011), but this has been challenged (Pichardo et al. 2012).

Previous studies of abundance trends in M67 have been based on small samples (e.g. Tautvaišiene et al. 2000; Yong et al. 2005; Randich et al. 2006; Pace et al. 2008; Pancino et al. 2010). In particular, Önehag et al. (2014), found that heavy elements abundances in dwarf stars are reduced by typically 0.05 dex or less, compared to in subgiants. Atomic diffusion has already been suggested as the underlying cause for the abundance trends in M67 (Önehag et al. 2014; Bertelli Motta et al. 2017); we note that, for the mass range of M67 (less than about 2 $M_{\odot}$), intermediate and heavy elements will not be influenced by nuclear reactions associated with dredge-up (Smiljanic et al. 2016); the light elements Li, Be, and B can be destroyed during the course of the first dredge-up.

However, in order to use the surface abundance trends to make quantitative statements about atomic diffusion processes, the measured surface abundances must be accurate. To date, most abundance analyses have employed the simplifying assumption of local thermodynamic equilibrium (LTE) for the gas in the stellar atmosphere. In reality, conditions in the line-forming regions are such that radiative transitions typically dominate over collisional transitions; the non-thermal radiation field thus drives the gas away from LTE. Thus, to measure surface abundances to better than 0.05 dex, departures from LTE must be taken into account (e.g. Asplund 2005, and references therein). Moreover, the errors arising from the assumption of LTE are systematic, and can therefore result in spurious abundance trends which, if taken to be real, can lead to incorrect conclusions about stellar and Galactic physics (e.g. sodium enhancement in open clusters; MacLean et al. 2015).

Here we present a detailed non-LTE abundance analysis of lithium, oxygen, sodium, magnesium, aluminium, silicon, and iron, across 69 M67 members. We employ a homogeneous data set drawn from the Galactic Archaeology with HERMES (GALAH) survey (De Silva et al. 2015), to study how departures from LTE can influence the observed abundance trends in M67. By comparing the trends against recent stellar models that include atomic diffusion, we investigate how departures from LTE influence interpretations about the efficiency of mixing processes in stellar atmospheres.

The rest of paper is structured as follows. In Sect. 2 we describe the observational data used in this study and the sample selection. In Sect. 3 we describe the abundance analysis. In Sect. 4 we present the inferred abundances and consider the abundance trends and the non-LTE effects. In Sect. 5 we discuss these results in relation to others in the literature, as well as to different models of stellar mixing. We conclude in Sect. 6.

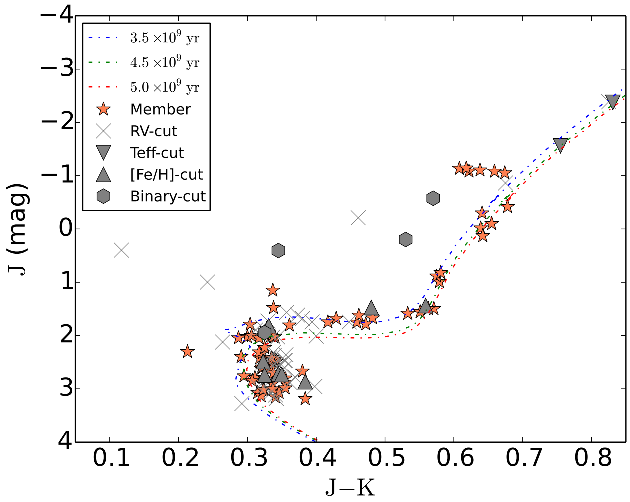

Figure 1. Colour-Magnitude Diagram of the open cluster M67 using the photometry data from 2MASS (Skrutskie et al. 2006). The excluded stars are represented by different grey symbols for different selection processes. The memberships selected and used in this study are marked as filled red asterisks. The spectroscopy binaries found in our final sample are shown in grey hexagon. The isochrones corresponding to an age of 3.5 Gyr, 4.5 Gyr and 5.0 Gyr are represented as dot-dashed lines in different colours.

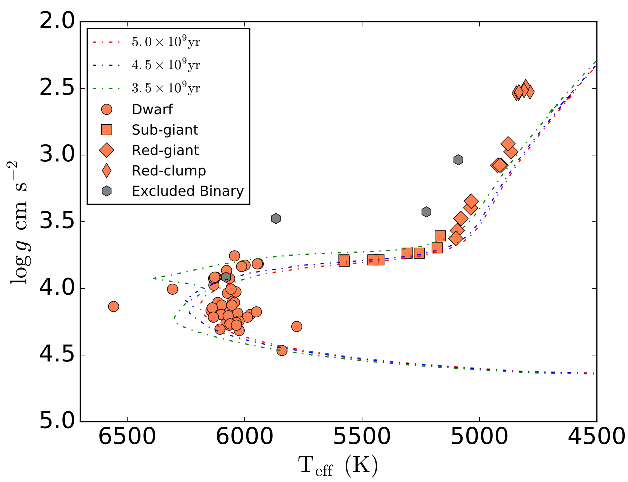

Figure 2. Theoretical isochrones of M67 with solar metallicity and different ages. The sample stars are divided into dwarfs, subgiants and giants represented by different symbols. Those excluded binaries are also been displayed. The effective temperature and gravity of our targeted stars has been added an offset of 46 K and 0.19 dex, respectively.

2 OBSERVATIONAL DATA AND SAMPLE SELECTION

The spectroscopic observations of target stars in M67 were taken from the GALAH survey, whose main science goal is to reveal the formation and evolutionary history of the Milky Way using chemical tagging (Freeman & Bland-Hawthorn 2002). The stars in the

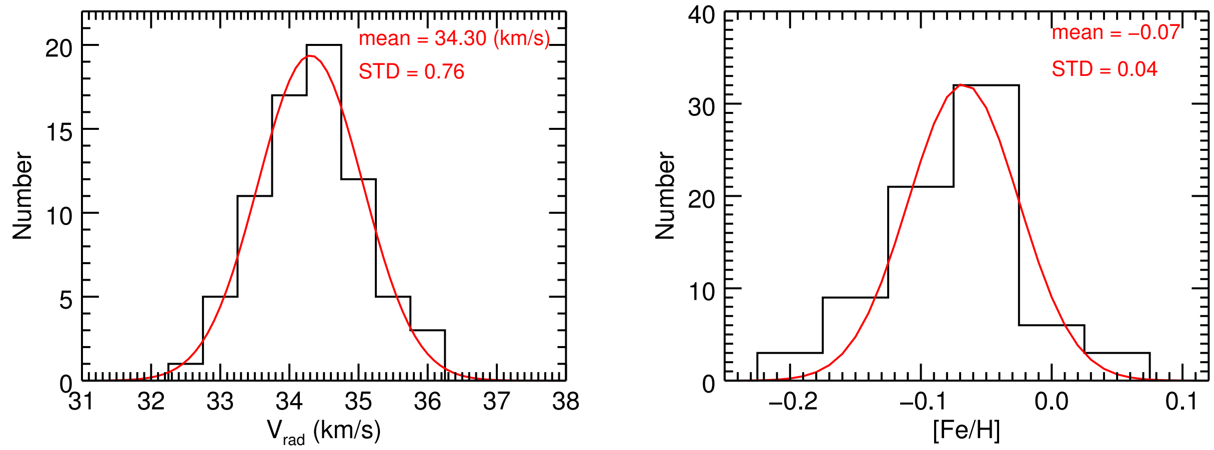

Figure 3. Histogram of the radial velocity and metallicity distributions of the final members selected in M67. The corresponding Gaussian fit to the distributions are also been shown in red lines.

GALAH survey were observed with the 2dF optical fibre positioner and HERMES spectrograph (Sheinis et al. 2015) mounted on the Anglo-Australian Telescope (AAT). The spectra provided by HERMES are in fixed format with four noncontiguous wavelength bands, 471.3-490.3 nm (Blue), 563.8-587.3 nm (Green), 647.8-673.7 nm (Red), and 758.5-788.7 nm (IR).

HERMES is designed to operate at two resolution modes for GALAH, having resolving powers of $R \sim 28,000$, the normal mode, and $R \sim 42,000$, which was only used during the GALAH pilot survey (Martell et al. 2017). This study is based only on spectra taken in the higher resolution mode (i.e. $R \sim 42,000$). The observations were carried out during the period of 7-14 February 2014. The exposure time ranges from 3600 s to 7200 s. The spectra were reduced using the dedicated GALAH reduction pipeline (Kos et al. 2017), with 2dfdr and IRAF used to perform bias subtraction, flat fielding, wavelength calibration, spectral extraction, and order merging. The sky background was subtracted from each individual observation. Observed spectra of the same object with different observation dates were stacked for higher signal-to-noise (SNR). All the objects satisfy SNR > 50 in Green, Red and IR arms.

In Fig. 1 we show the colour-magnitude diagram (CMD) containing the initial sample. The initial observed targets are selected based on the Two Micron All Sky Survey (2MASS) Catalogue using JHK photometry (Skrutskie et al. 2006) to estimate V(J,K) to define our target selection criteria, with a baseline selection corresponding to $8.8 < V < 14$. We determined the radial velocities and spectroscopic stellar parameters as described in Sect. 3.3. To refine the membership selection, we iteratively rejected $2\,\sigma$ outliers in radial velocity. We also excluded two probable members that are cooler than 4500 K, since the spectroscopic method we adopt (using unblended H and Fe lines) is not reliable at these cool temperatures. Finally, we retained all the stars within $3\,\sigma$ in [Fe/H] as our final sample, thereby rejecting another 8 probable foreground objects of similar radial velocity as the cluster. The abandoned and retained stars are shown in different symbols in Fig. 1.

In Fig. 3 we show the histograms of the radial velocity and metallicity distributions of the final sample of stars, together with a Gaussian fit with RV = 34.30 and $\sigma = 0.76$, which is basically consistent with the result from Geller et al. (2015) (RV = 33.64 ± 0.96). We also made a cross-match of our targeted stars on SIMBAD (Wenger et al. 2000) by using the coordinates to identify the corresponding objects within a radius of 2 arcsec. We found four stars in our final sample (marked as grey hexagon in Fig. 1) that have been verified as spectroscopic binaries on SIMBAD; we excluded these binaries in the sample. We also see that six stars stand out in Fig. 1 as likely red clump stars. The final stellar sample contains 69 stars with high resolution spectra, including post main-sequence, turn-off, subgiant, giant, and red clump stars.

3 ABUNDANCE ANALYSIS

The spectra were analysed using a modified version of the GALAH analysis pipeline, which is developed for a full scientific analysis of the GALAH survey and has been applied to determine stellar parameters and abundances in many recent studies (e.g. Sharma et al. 2017; Wittenmyer et al. 2017; Duong et al. 2018). The pipeline will be further described and the results for the full survey sample evaluated in GALAH's second data release paper to appear soon (Buder et al. in prep.). The input data for this pipeline includes: the reduced observed spectra and corresponding measurement errors (Sect. 2); initial guesses for the stellar atmosphere parameters and radial velocity; reference solar abundances; and a list of atomic and molecular lines. The spectra, which have been radial velocity corrected as described in Kos et al. (2017), were first continuum-normalised using straight lines over 3-60 Å wide segments in all four arms. Wavelength regions contaminated by telluric or sky lines were removed (Buder et al 2018). The radiative transfer and abundance analysis was carried out using the automated spectrum analysis code Spectroscopy Made Easy (sme; Piskunov & Valenti 2017) We detail aspects of this pipeline in the remainder of this section.

3.1 Atmosphere grids

The spectral line synthesis with sme is based on marcs model atmospheres (Gustafsson et al. 2008) with atmospheric parameters spanning effective temperatures $2500 \leq T_{\rm eff}/{\rm K} \leq 8000$, surface gravities $-0.5 \leq \log_{10}\left(g/{\rm cm\,s^{-2}}\right) \leq 5.0$, and metallicities $-5.0 \leq$ [Fe/H] ≤ 1.0. Spherical models were used for $\log g \leq 3.5$ and plane-parallel models were otherwise used. The standard chemical composition grid was adopted, which uses the solar chemical composition of Grevesse et al. (2007), scaled by [Fe/H] and with an enhancement to α-elements of 0.1 dex for [Fe/H] = −0.25, 0.2 dex for [Fe/H] = −0.5, 0.3 dex for [Fe/H] = −0.75, and 0.4 dex for [Fe/H] ≤ −1.0.

3.2 Non-LTE grids

For non-LTE calculations in SME, instead of solving the non-LTE radiative transfer equations directly, grids of pre-computed departure coefficients $\beta = n_{\rm NLTE}/n_{\rm LTE}$ as functions of optical depth were employed instead, as described in Piskunov & Valenti (2017). When performing the spectral fitting for stellar parameter determinations, as well as the spectral fitting for chemical abundance determinations, the grids of pre-computed departure coefficients (for each stellar model and target abundance) were read in and interpolated based on a given stellar model and non-LTE abundance, then applied to the corresponding LTE level populations to synthesise the lines. It is worth to mention that we found a bug in non-LTE oxygen lines synthesis. We therefore have a different treatment for getting non-LTE oxygen abundances, i.e. applying directly non-LTE correction to oxygen abundances that are obtained from synthesizing the lines in LTE. This is also a common and justifiable way to be used in 3D non-LTE correction calculations.

The non-LTE departure coefficient grids for all the elements were taken from recent non-LTE radiative transfer calculations based on 1D hydrostatic model MARCS atmospheres (i.e. consistent with the rest of the analysis). The calculations themselves, and/or the model atoms, were presented in the following studies:

- lithium: Lind et al. (2009a)
- oxygen: Amarsi et al. (2015) (model atom)
- sodium: Lind et al. (2011)
- magnesium: Osorio & Barklem (2016)
- aluminium: Nordlander & Lind (2017)
- silicon: Amarsi & Asplund (2017) (model atom)
- iron: Amarsi et al. (2016b)

We refer the reader to those papers for details on the model atoms; we only provide a brief overview here.

Energy levels and radiative data were taken from various databases, as appropriate or applicable: NIST (Reader et al. 2012), TOPbase (Peach et al. 1988), TIPbase (Bautista 1997), and the Kurucz online datebase (Kurucz 1995). Inelastic collisional processes, between the species in question and either free electrons or neutral hydrogen atoms, can be a major source of uncertainty in non-LTE analyses (e.g. Barklem 2016a). The oxygen, sodium, magnesium and aluminium grids benefit from X+e inelastic collision data based on the R-matrix method (e.g. Burke et al. 1971; Berrington et al. 1974), which is more reliable than commonly used alternatives, such as the van Regemorter recipe (van Regemorter 1962). Furthermore, all seven grids benefit from X+H inelastic collision data based on the asymptotic two electron model of Barklem (2016b), that is in turn more reliable than the commonly used Drawin recipe (Steenbock & Holweger 1984; Lambert 1993).

3.3 Spectroscopic stellar parameters

To avoid degeneracy issues that result from having too many free model parameters, the analysis separates the determination of the surface elemental abundances from the rest of the stellar parameters, namely the atmospheric parameters $T_{\rm eff}$, $\log g$, [Fe/H], as well as projected rotational velocities $\upsilon \sin \iota$, and line-of-sight radial velocity $v_{\rm rad}$. In addition, microturbulence ξ and macroturbulence $\upsilon_{\rm mac}$ are standard parameters in 1D atmosphere analysis used to model the impact of convective motions on the spectral lines (e.g. Gray 2005, Chapter 17). An empirical relation for ξ as a function of $T_{\rm eff}$ (see Fig. 4) and $\log g$ was derived and adopted, while $\upsilon_{\rm mac}$ was implicitly accounted for within $\upsilon \sin \iota$, as the latter was treated as a free parameter. During this procedure, the input spectra have also been convolved with a Gaussian instrumental profile of varying resolution over each arm, which is the dominant source of broadening.

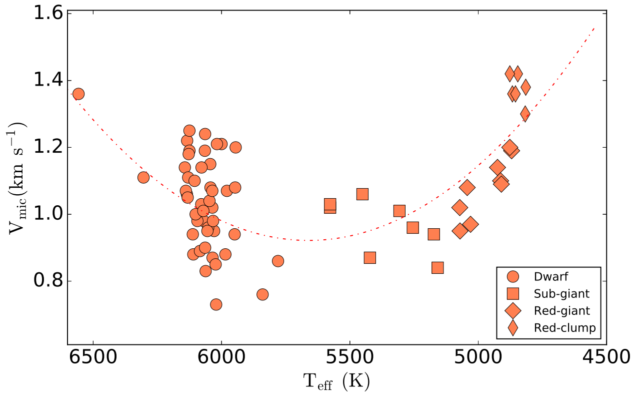

Figure 4. Microturbulence ξ as a function of effective temperature, when treated as a free parameter in stellar parameters calculation. This distribution was fitted by an empirical quadratic polynomial, in order to determine the relation between these two parameters which was subsequently enforced.

The stellar parameters were determined simultaneously, by fitting (via χ^2 minimisation) the observed profiles of Sc I, Sc II, Ti I, Ti II, Fe I, and Fe II lines that were unblended and that had reliable atomic data, as well as two of the Balmer lines: Hα and Hβ. The benefit of this approach is that, for example, both the temperature sensitive Balmer line wings and the excitation-balance of neutral iron-peak species strongly influence the effective temperature determination; similar statements can be made for the inferred surface gravity and metallicity (Sect. 3.2). In this process, iron was generally treated in non-LTE (Amarsi et al. 2016b); since the non-LTE effects on neutral iron lines are small, for late-type stars of solar-metallicity (e.g. Lind et al. 2017), we find this choice has only a small influence on the values of the other stellar parameters (the mean differences in $T_{\rm eff}$ and $\log g$ under LTE and non-LTE are 3.5 K and 0.01 dex, respectively).

By analyzing the high resolution spectrum of solar (Sect. 3.5), we find that our analysis pipeline requires some small offsets in $T_{\rm eff}$, $\log g$ and [Fe/H] of 46 K, 0.19 dex and 0.07 dex respectively, to match the reference solar values. Following other large spectroscopic surveys, such as in APOGEE (Holtzman et al. 2015, Sect. 5) and RAVE (Kunder et al. 2017, Sect. 6), we applied these offsets directly to all the other stars in our sample for the stellar parameters calibration. we stress that this amount of change to the stellar parameters does not have a strong influence on our inferred elemental abundances.

As a sanity check, in Fig. 2 we compare our effective temperatures and surface gravities with theoretical cluster isochrones. The three stellar evolutionary tracks and isochrones have been produced by Padova database (Bressan et al. 2012; Chen et al. 2014;

Table 1. Comparison of solar abundances with respect to the standard composition of MARCS model atmospheres.

Element	Non-LTE	LTE	Grevesse et al. (2007)
Li	0.99 ± 0.04	0.98 ± 0.04	1.05 ± 0.10
O	8.73 ± 0.07	8.89 ± 0.07	8.66 ± 0.05
Na	6.17 ± 0.09	6.31 ± 0.09	6.17 ± 0.04
Mg	7.60 ± 0.03	7.58 ± 0.03	7.53 ± 0.09
Al	6.43 ± 0.02	6.45 ± 0.02	6.37 ± 0.06
Si	7.45 ± 0.02	7.46 ± 0.02	7.51 ± 0.04
Fe	7.46 ± 0.03	7.44 ± 0.02	7.45 ± 0.05

Tang et al. 2014), with solar metallicity (Z = 0.0142), but different ages of t = 3.5 Gyr, t = 4.5 Gyr (close to that of the Sun), and t = 5.0 Gyr. The parameters of the stars fall into the reasonable region of the isochrone tracks, without any further calibrations.

3.4 Spectroscopic abundances

In principle, GALAH spectra can allow for up to 30 elements to be determined, but here we only focus on those that we have non-LTE grids for. Having obtained the optimal stellar parameters (Sect. 3.3), elemental abundances for lithium, oxygen, sodium, magnesium, aluminium, and silicon were then inferred; the abundance of iron was also re-inferred, using only iron lines. The trace element assumption was employed here: i.e. that a small change to the abundances of the particular element being studied has a negligible impact on the background atmosphere and hence the optimal stellar parameters. Thus, the stellar parameters were kept fixed, and the only free parameters were the elemental abundances. The synthesis of the spectral lines incorporated non-LTE departure coefficients (Sect. 3.2).

Unsaturated, unblended lines are preferred as abundance indicators. For partially blended lines in the list, synthetic spectra are fitted in an appropriate selected spectra region that neglects the blended part of the line. Likewise, the abundances were calculated from those lines using χ^2 minimised synthetic fits. All of the lines used in the abundance analysis and their detail information will be shown in Buder et al. in prep. Fig. 5 shows the comparison between observed and best-fit synthetic line profiles of Na, Mg and Si in both LTE and non-LTE for three stars coming from different groups: dwarfs, subgiants and giants.

3.5 Solar reference

In order to obtain accurate abundance ratios of these late-type stars with respect to the Sun, it is important to determine solar abundances in a consistent manner (e.g. García Pérez et al. 2006). However, we do not have access to a high-quality HERMES solar spectrum observed in the high-resolution mode. Instead, we used the very high-resolution ($R \sim 350,000$) Kitt Peak solar flux atlas of Brault & Neckel (1987). The solar analysis proceeded in the same way as for our M67 targets. The resulting spectroscopic parameters are generally in good agreement with the standard solar values, with some small offsets for the spectroscopic $T_{\rm eff}$ to be lower by 46 K, log g to be lower by 0.19 dex, and [Fe/H] to be 0.07 dex, as we already mentioned in Sect. 3.3 The above offsets were applied to the subsequent solar abundance analysis, as well as to the abundance analysis of M67 stars.

We list the final inferred solar abundances in Table 1. Our solar abundances are in good agreement with those of Grevesse et al. (2007), the most discrepant elements being magnesium and oxygen, both of which are 0.07 dex higher in our non-LTE analysis. Our solar abundances are also very similar to the 1D non-LTE ones presented in Scott et al. (2015); all of our values agree with theirs to within 0.04 dex.

4 RESULTS

We present and discuss the results here. First, we divide our sample into dwarf stars ($T_{\rm eff;\,DW}$ > 5800 K), subgiant stars (5100 K < $T_{\rm eff;\,SUB}$ < 5800 K), and giant stars ($T_{\rm eff;\,RGB}$ < 5100 K); in Fig. 6 we plot the mean [X/H] abundances for the three groups. In Fig. 7 and Fig. 8 we plot LTE and non-LTE abundances of individual M67 stars as a function of effective temperature. We discuss different aspects of these plots in the remainder of this section.

4.1 Influence of departures from LTE

In Fig. 6 we compare the mean LTE and non-LTE [X/H] abundances, for three groups of the cluster stars: dwarf stars, subgiant stars and giant stars. These were calculated consistently by treating iron in LTE/non-LTE when determining the stellar parameters, and by using our LTE/non-LTE solar reference values. For the dwarf stars, under LTE, we find a peculiarly large overabundance in [O/H] of more than 0.15 dex, compared to the other species. This is a non-LTE effect; under non-LTE, the abundance ratios [X/H] for the different elements are all consistent with each other. For the subgaint stars, both LTE and non-LTE abundance results are generally consistent with each other. This group also gives results closest to solar (i.e. [X/H] = 0) than the other two groups. For the giant stars, there is a large difference in the abundances [X/H] between different elements, in both LTE and non-LTE. However, due to the large error bars of most elements, we can not draw a strong conclusion about this, even though this scatter of the abundance pattern is smaller under non-LTE than under LTE.

In Fig. 7 we show LTE and non-LTE abundances as a function of effective temperature for individual member stars of M67. Here, both LTE and non-LTE abundances were calculated by treating iron in non-LTE when determining the stellar parameters, and were put onto a relative ([X/H]) scale using our non-LTE solar reference. This illustrates the departures from LTE in the absolute abundances, as a function of effective temperature. We discuss the departures from LTE for different elements separately, in the following subsections.

4.1.1 Lithium

Lithium abundances were determined from the resonance LiI 670.8 nm doublet . For lithium-poor stars (A(Li) < 2), it was impossible to obtain lithium abundances because of the very weak line strength. Most stars cooler than 5900 K are in this category, as they have suffered strong lithium depletion; an added complication in cooler stars is that the doublet is seriously blended with a nearby FeI line. we found one exception at $T_{\rm eff} \approx 5600$ K, a lithium-rich subgiant (Sect. 4.2). This star was among the ones that were rejected as members via the radial velocity criterion. The lithium abundances in the sample are largely insensitive to departures from LTE (see Fig. 8), and the mean Li abundances for non-LTE and LTE calculations are identical and have the same standard deviation: A(Li) = 2.42 ± 0.17.

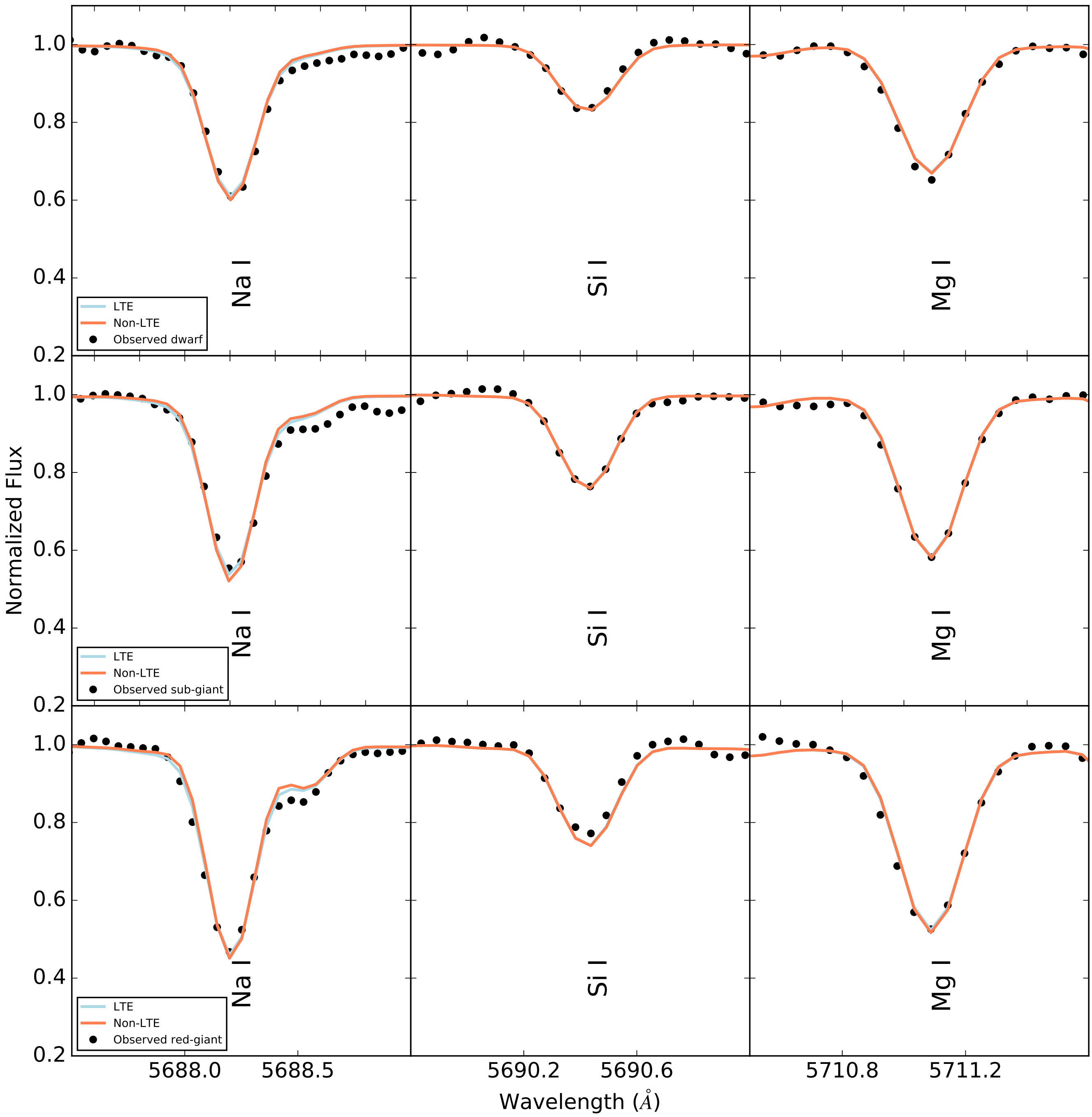

Figure 5. Typical best-fit synthetic LTE and non-LTE line profiles of Na, Mg and Si compared with the observed spectra of three stars in different evolutionary stage; a dwarf, a subgiant and a giant.

The scatter in our lithium abundances (for those warmer stars in which the doublet could be measured) is large. The observed spread in our lithium abundance for stars around solar mass range has also been reported by other studies (Pasquini et al. 2008; Pace et al. 2012). The fundamental parameters of these dwarfs (mass, metallicity and age) should be similar; it is possible however that they were born with different initial angular momenta, which is one of the key paers for rotational mixing, leading to different lithium depletions between these otherwise similar stars (Pinsonneault 2010).

All of the dwarfs in the M67 sample in which we detect lithium have effective temperatures larger than $T_{\rm eff} \approx 5900$ K; in these hot dwarfs layers, the combination of overpopulation in the Li ground state and superthermal source function make the non-LTE abundance corrections appproximately zero for this line (e.g. Lind et al. 2009a).

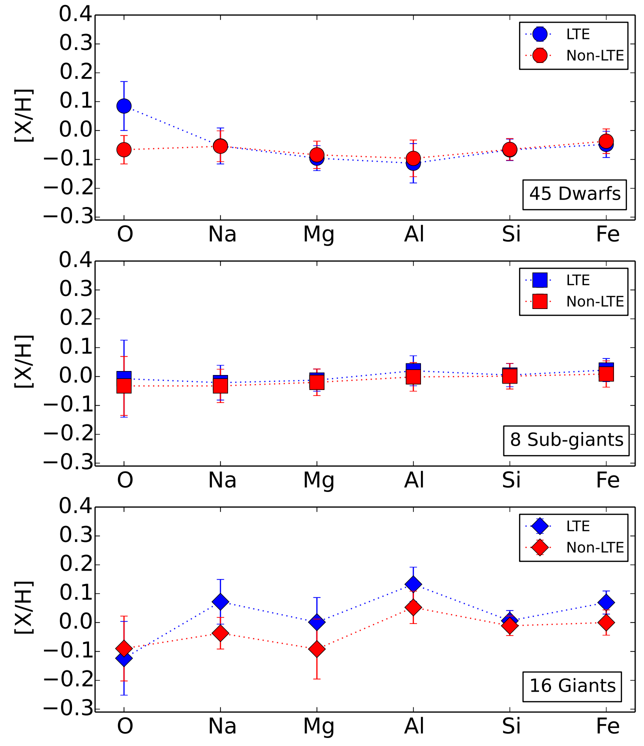

Figure 6. Abundance patterns of dwarf, subgiant and giant stars in our final sample. LTE/non-LTE [X/H] values were calculated consistently by treating iron in LTE/non-LTE when determining the stellar parameters, and by using our LTE/non-LTE solar reference values. Each symbol represents the mean abundance [X/H] of that group stars, and the error bars correspond to the standard deviation in that group.

4.1.2 Oxygen

Oxygen abundances were determined from the O I infra-red triplet, its three components located at 777.19 nm, 777.42 nm, and 777.54 nm. The mean non-LTE and LTE abundances of oxygen are $[\mathrm{O/H}]_{\mathrm{NLTE}} = -0.07 \pm 0.08$ and $[\mathrm{O/H}]_{\mathrm{LTE}} = 0.21 \pm 0.11$. The difference between the oxygen abundances using non-LTE and LTE synthesis are large ($\Delta_{\mathrm{non-LTE-LTE}} \approx -0.28$ dex). The small line strengths in giant stars and imperfect correction for telluric contamination result in larger star-to-star scatter compared to the other elements studied here, even when LTE is relaxed.

The departures from LTE are mainly due to photon losses in the lines themselves, which leads to an overpopulation of the metastable lower level, and the increased line opacity strengthens the line in non-LTE (e.g. Kiselman 1993; Takeda 2003; Amarsi et al. 2016a). As clearly seen in Fig. 7 the non-LTE abundance corrections are larger in dwarfs (at higher T_{eff}) than in giants (at lower T_{eff}). This is expected, because the oxygen triplet gets stronger with effective temperature, increasing the photon losses in the lines themselves and hence making the departures from LTE more severe.

4.1.3 Sodium

Sodium abundances were determined from the Na I doublet, its components located at 568.26 nm and 568.82 nm. Additionally, the Na I 475.18 nm line was available for a part of the sample. The mean non-LTE and LTE abundances of sodium are $[\mathrm{Na/H}]_{\mathrm{NLTE}} = -0.05 \pm 0.06$ and $[\mathrm{Na/H}]_{\mathrm{LTE}} = 0.13 \pm 0.07$. Non-LTE effects evidently play an important role in Na line formation and cause a substantial negative correction ($\Delta_{\mathrm{non-LTE-LTE}} \approx -0.18$ dex).

The departures from LTE in optical NaI lines are largely driven by photon suction in strong lines, in particular the Na D resonance lines (NaI 588.9 rm and Na I 589.5 nm). A recombination ladder from the Na II reservoir tends to cause overpopulations of lower states and subthermal source functions, resulting in negative abundance corrections that are strongest for saturated lines (e.g. Lind et al. 2011).

4.1.4 Magnesium

Magnesium abundances were determined from the MgI 473.30 nm, the Mg I 571.11 nm, and the Mg I 769.16 nm. The mean non-LTE and LTE abundances of magnesium are $[\mathrm{Mg/H}]_{\mathrm{NLTE}} = -0.08 \pm 0.07$ and $[\mathrm{Mg/H}]_{\mathrm{LTE}} = -0.07 \pm 0.07$. Although the impact of departures from LTE is not very pronounced on the mean abundances, it is interesting to note there is still a clear influence on the abundance trends. This is because the giants tend to have negative abundance corrections, whereas the dwarfs tend to have positive abundance corrections.

The physical non-LTE effect is different in dwarfs and giants. In dwarf stars, the photoionisation rates for the lower Mg I levels are substantial, which can lead to overionisation, resulting in positive non-LTE abundance corrections. In contrast, in giant stars, MgI lines (especially the Mg I 571.11 nm line) suffer from photon losses, making the abundance corrections negative (e.g. Osorio et al. 2015; Bergemann et al. 2017).

4.1.5 Aluminum

Aluminium abundances were determined using the doublet: Al I 669.6 nm and Al I 669.8 nm. The mean non-LTE and LTE abundances of aluminium are $[\mathrm{Al/H}]_{\mathrm{NLTE}} = -0.06 \pm 0.09$ and $[\mathrm{Al/H}]_{\mathrm{LTE}} = -0.03 \pm 0.11$. The very weak aluminium lines in dwarfs cause a substantial abundance scatter. In addition, the doublet falls in a spectral region where the wavelength calibration of HERMES is of lower quality, which manifests itself in poor synthetic fits to the observed spectral lines. To improve this defect, we set radial velocity as a free parameters as well when carrying out spectra synthesis of aluminium; this unfortunately further contributes to the abundance scatter.

The non-LTE abundance correction are always negative and become much more severe in giants than the corrections in dwarfs. The negative sign of the corrections is due to photon suction effects, resulting in overpopulations of lower levels and subthermal source functions. These effects are strongest in giants. Towards warmer effective temperatures, the non-LTE effect starts to change: a larger supra-thermal UV radiation field means that a competing overionisation effect becomes more efficient. As such, the non-LTE abundance corrections are much less less severe in dwarfs.

4.1.6 Silicon

Five silicon lines were used to determine silicon abundances: Si I 566.55 nm, Si I 569.04 nm, Si I 570.11 nm, Si I 579.31 nm, and Si I 672.18 nm. The mean non-LTE and LTE abundances of silicon are $[\mathrm{Si/H}]_{\mathrm{NLTE}} = -0.05 \pm 0.05$ and $[\mathrm{Si/H}]_{\mathrm{LTE}} = -0.03 \pm 0.05$.

The non-LTE abundance corrections for Si lines are not very pronounced, however they are always negative in this sample.

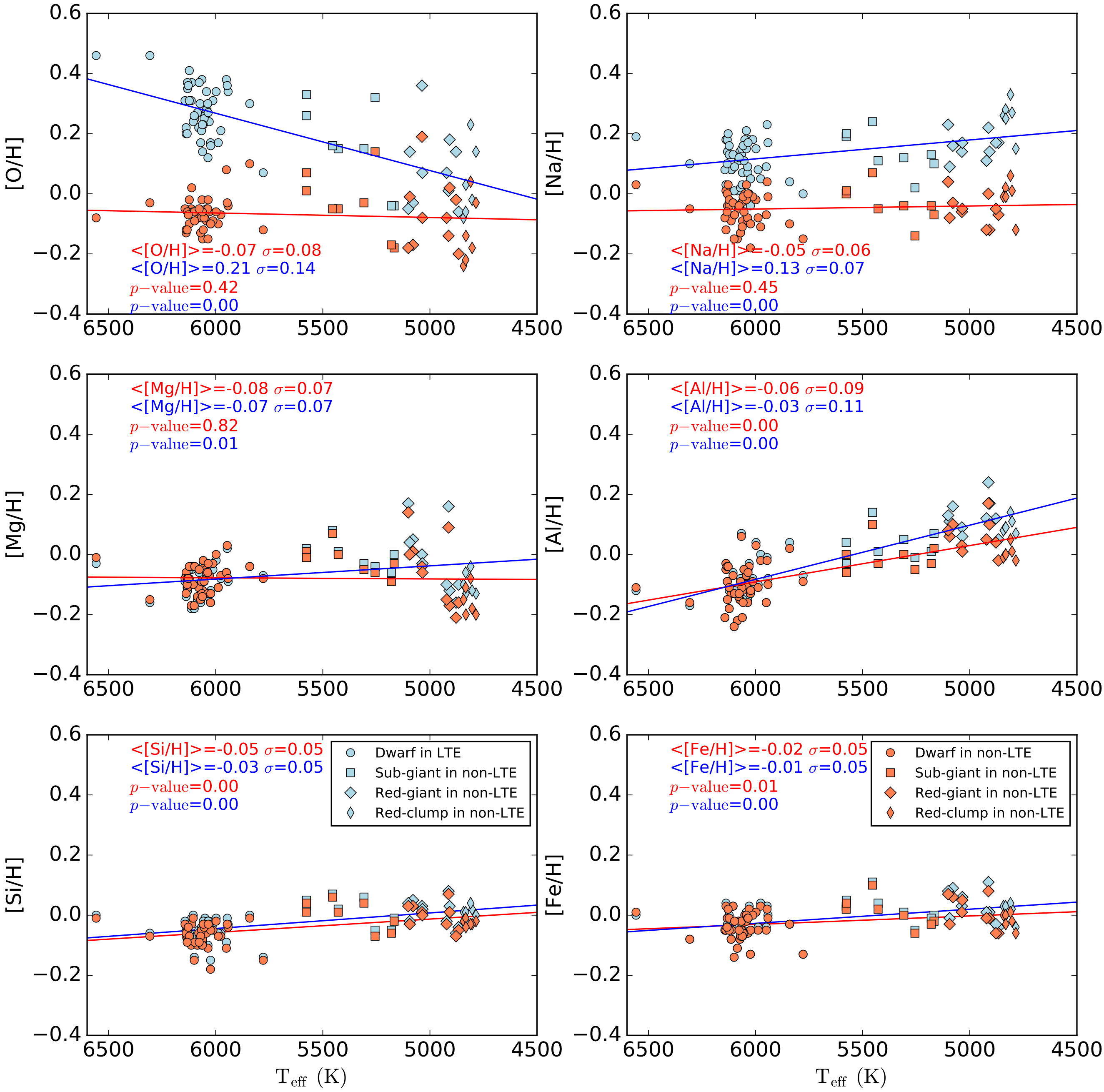

Figure 7. LTE and non-LTE abundances as a function of effective temperature for individual member stars of M67. All LTE and non-LTE abundances shown here were calculated by treating iron in non-LTE when determining the stellar parameters, and were put onto a relative ([X/H]) scale using our non-LTE solar reference. Stars with different evolutionary states are marked using different symbols. The *p*-values of the trends in LTE and non-LTE are shown in the legends, where a small value (typically *p*-value $\lesssim 0.05$) is indicative that the trend is significant with respect to the scatter.

Generally, photon losses in the Si I lines drives overpopulation for the lower levels and underpopulation for higher levels, which strengthen the lines in non-LTE.

4.1.7 Iron

Iron abundances were determined by a selection of Fe I and Fe II, that will be listed in Buder et al. in prep. The mean non-LTE and LTE abundances of iron are $[Fe/H]_{NLTE} = -0.02 \pm 0.05$ and $[Fe/H]_{LTE} = -0.01 \pm 0.05$. Non-LTE effects cause a small negative correction ($\Delta_{non-LTE-LTE} \approx -0.03$ dex).

Since Fe II lines are almost immune to non-LTE effects in late-type stars (at least, in 1D hydrostatic model atmospheres such as those used in this work – in 3D hydrodynamic model atmospheres and in reality this is not always the case; e.g. Amarsi et al. 2016b, Table 3), the main contribution to the difference between the mean abundances under LTE and non-LTE comes from the Fe I lines. The traditional non-LTE effect for Fe I lines is overionisation; at

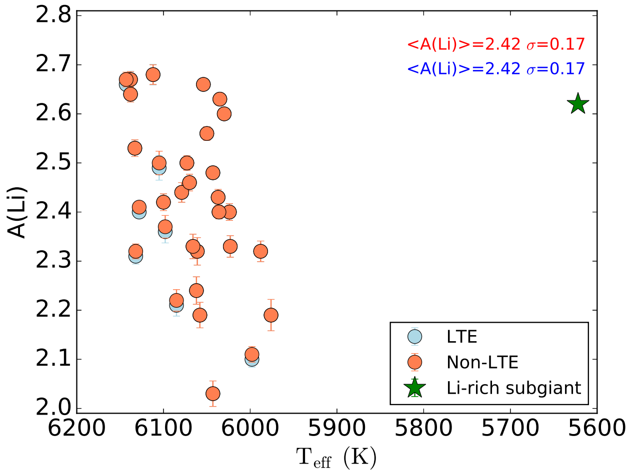

Figure 8. Absolute abundance distributions of lithium as a function of effective temperature. A lithium-rich subgiant located in a binary system, which we ruled out via our our radial velocity criterion, is marked using an asterisk.

solar-metallicity, however, this effect is relatively small, and photon losses in the Fe I lines as well as a general photon-suction effect are more important. We therefore see slightly negative abundance corrections. The effects are more severe in giants, where these intermediate-excitation Fe I lines are stronger.

4.2 Lithium-rich subgiant

Among the full sample of stars observed in the M67 field, we discovered a subgiant star with a very high lithium abundance A(Li) = 2.6 (see Fig. 8). However, because of its radial velocity, $v_{\rm rad}$ = 38.5 km s^{-1}, which is high compared to the cluster mean (see Fig. 3), we regard this star as a potential non-member and have excluded it from the discussion of cluster abundance trends. No other subgiant star in the sample has such a high lithium abundance, and severe lithium depletion is expected at this evolutionary stage after leaving the main sequence turn-off (Balachandran 1995; Pace et al. 2012). By checking the position and magnitude information, this star has been confirmed as a spectroscopy binary on the SIMBAD.

Canto Martins et al. (2006) also reported a lithium-rich subgiant star S1242 with (A(Li) = 2.7). S1242 has been verified as a member of a large eccentricity binary system in M67, with a faint low-mass dwarf companion providing negligible contribution to the luminosity (Sanders 1977; Mathieu et al. 1990). Canto Martins et al. (2006) proposed that high chromospheric activity and unusually high rotational velocity of S1242, may be induced by tidal interaction, which can help the star conserve its lithium abundance from the turn-off stage. Interestingly, Önehag et al. (2014) also found a lithium-rich subgiant star S1320 with A(Li) = 2.3. This subgiant has been included in their membership, since they did not find any evidence that this star has been contaminated by a companion.

4.3 Abundance trends

As illustrated in Fig. 7, we have found abundance trends with effective temperature for some elements. The trends are more pronounced when LTE is assumed; furthermore, the scatter around the mean for oxygen becomes more pronounced when LTE is assumed. Even under non-LTE, however, there still exist some systematic abundance differences between dwarfs, subgiants and giants, as can be seen in Fig. 7.

To determine if there is a significant correlation between element abundance and effective temperature, we calculate *p*-values in the linear regression analysis by assuming there is no correlation between these two parameters in the null hypothesis. The *p*-values of the trends are shown in the legends of Fig. 7, where a small value (typically *p*-value $\lesssim$ 0.05) is indicative that the trend is significant with respect to the scatter. We can thus say that, under LTE, the trends in surface abundance against effective temperature are significant with respect to the scatter, for all of the species shown in Fig. 7. In contrast, under non-LTE, the trends for oxygen, sodium and magnesium are not significant with respect to the scatter; for iron the trend is marginally significant (*p*-value $\approx$ 0.01), while for aluminium and silicon the trends remain obviously significant.

In summary, non-LTE analysis tends to flatten the trends with effective temperature seen in LTE, which reduces the scatter in mean abundance for most elements. The remaining residual trends may reflect other systematic errors still present in the analysis or the true surface composition of the stars. If real, such trends may be explained by stellar evolution under the impact of atomic diffusion. We shall consider this in more detail in Sect. 5.2.

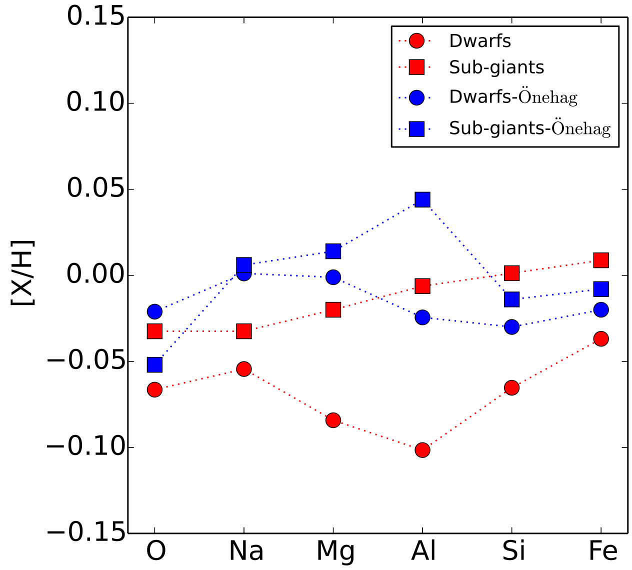

Figure 9. A comparison between our non-LTE abundance patterns of dwarf, subgiant and giant stars and those from Önehag's dwarf and early subgiant stars.

5 DISCUSSION

5.1 Comparison to other studies

In this section, we compare our abundance results to previous high-resolution studies of M67. Table 2 summarises the target selection and spectroscopic quality for seven literature studies. We also include the mean abundance ratios determined in those studies. We compare these results, which were mainly based on equivalent-widths and under LTE, with our own results, which are based on spectral line fitting and under non-LTE.

Table 2. The comparison of average abundances in common for M67 based on high resolution spectroscopy. The total number of stars analyzed in each study is given by N.

	This work (NLTE)	T00[1]	Y05[2]	R06[3]	P08[4]	P10[5]	F10[6]	Ö14[7]
N	69	9	3	10	6	3	3	14
R	42000	30000–60000	28000	45000	100000	30000	30000	50000
SNR	50–150	≥ 100	30–100	90–180	≃ 80	50–100	150–180	150
[Fe/H]	−0.02 ± 0.05	−0.03 ± 0.03	+0.02 ± 0.14	+0.03 ± 0.03	+0.03 ± 0.04	+0.05 ± 0.02	+0.03 ± 0.07	−0.02 ± 0.04
[O/Fe]	−0.01 ± 0.09	+0.02 ± 0.06	+0.07 ± 0.05	+0.01 ± 0.03	−0.07 ± 0.09	+0.04 ± 0.10	−0.16 ± 0.05	−0.02 ± 0.05
[Na/Fe]	+0.01 ± 0.05	+0.19 ± 0.06	+0.30 ± 0.10	+0.05 ± 0.07	−0.02 ± 0.07	+0.08 ± 0.09	+0.13 ± 0.10	+0.02 ± 0.03
[Mg/Fe]	−0.02 ± 0.05	+0.10 ± 0.04	+0.16 ± 0.08	+0.00 ± 0.02	-	+0.27 ± 0.04	+0.05 ± 0.03	+0.02 ± 0.02
[Al/Fe]	+0.01 ± 0.06	+0.14 ± 0.04	+0.17 ± 0.05	−0.05 ± 0.04	−0.03 ± 0.11	+0.03 ± 0.02	+0.11 ± 0.07	+0.02 ± 0.04
[Si/Fe]	+0.01 ± 0.03	+0.10 ± 0.05	+0.09 ± 0.11	+0.02 ± 0.04	−0.03 ± 0.06	+0.10 ± 0.02	+0.18 ± 0.04	−0.01 ± 0.02

Notes. (1) Tautvaišiene et al. (2000) analysed 6 red clump stars and 3 gaint stars. (2) Yong et al. (2005) analysed 3 red clump stars. (3) Randich et al. (2006) analysed 8 dwarfs and 2 slightly evolved stars. (4) Pace et al. (2008) analysed 6 main-sequence stars. (5) Pancino et al. (2010) analysed 3 red clump stars. (6) Friel et al. (2010) analysed 3 red clump stars. (7) Önehag et al. (2014) analysed 14 stars whose 6 are located on the main sequence, 3 are at the turn-off point, and 5 are on the early subgiant branch.

Our mean [Fe/H] value in non-LTE for M67 is consistent with the value of Tautvaišiene et al. (2000) and Önehag et al. (2014), but is slightly lower than those determined from the other studies shown in Table 2. Generally all the results are comparable with solar metallicity to within their respective errors. However, some disagreements between other measured abundances from different studies do exist.

Overall, our abundance ratios in non-LTE are close to solar, and are systematically lower than those studies wherein only giants have been analyzed, namely Tautvaišiene et al. (2000) , Yong et al. (2005), Pancino et al. (2010) and Friel et al. (2010). The abundance results that are based mainly on unevolved stars from Randich et al. (2006), Pace et al. (2008) and Önehag et al. (2014) are more consistent with ours.

The abundance differences seen between ours and other studies can be caused by many factors, such as, atmospheric model, abundance calculation code, the determined stellar parameters, the choice of log gf values and line lists, the choice of solar reference abundances and non-LTE effects. Here all our abundances are determined by spectrum synthesis, which are more reliable and accurate especially when the lines are blended than the traditional EW analysis. Besides, we have a largest sample with high quality spectra covering post main-sequence, turn-off, sub-giant star, red giant and red clump stars compared with other studies, whose abundances are derived based on a small number of objects.

We compare the results of Önehag et al. (2014) with ours in Fig. 9. These authors analysed 14 dwarfs and subgiants using high resolution spectra ($R \approx 50,000$), an analysis based on equivalent-widths and under LTE. Their abundances were derived for each spectral line individually relative to those of the solar proxy M67-1194. Our mean chemical abundances are typically lower than the ones from Önehag et al. (2014). However, in that work as well as our own, we find that the abundances in subgiants are enhanced relative to those in dwarfs. This enhancement is smaller in the results of (Önehag et al. 2014) than in this work; this is likely because the subgiants used in that work are located very close to the turn-off, whereas here they are span all the way to the giant phase. This overall increasing abundances from dwarfs to subgiants could be a signature for possible diffusion process (Sect. 5.2).

Table 3. Offsets are applied to the stellar evolution model abundances.

Element	$[X/H]_{offset}$
O	0.01
Na	0.01
Mg	0.11
Si	0.03
Fe	−0.05

5.2 Comparison with atomic diffusion models

Atomic diffusion is a continuous process whose influence immediately below the outer convection zone cause surface abundance variations during the main-sequence phase of a star. At the turn-off point, where the convective envelope is the thinnest, the settling of elements reaches a maximum. As the star evolves along the subgaint branch and red giant branch, the surface abundances begin to recover gradually to the initial value due to the enlarged surface convection zone, except for those light elements that are affected by nuclear processing.

The metals in our Sun are thought to be underabundant relative to the initial bulk composition, by about 0.04 dex (e.g. Asplund et al. 2009). Turcotte et al. (1998) demonstrated that the diffusive process is dominant at the end of main-sequence phases of solar-type stars, thus the turnoff stars in M67 with comparable age to the Sun may show even larger effects of atomic diffusion. Larger effects are also expected in warm metal-poor stars, because of their older ages and thinner surface convection zones (Michaud et al. 1984).

Our sample includes stars in different evolutionary states, including post main-sequence, turn-off, subgiant, red giant branch and red clump. It is therefore of interest to compare our results with those predicted by stellar evolutionary models that include atomic diffusion. We adopted the surface abundances that were calculated in Dotter et al. (2017) with solar metallicity, initial masses ranging from $0.5M_{\odot}$ to $1.5M_{\odot}$ and ages of $t = 4.0$ Gyr, $t = 4.5$ Gyr and $t = 5.0$ Gyr, respectively. The stellar evolutionary models (MIST; Dotter 2016; Choi et al. 2016) have included atomic diffusion, overshooting mixing and turbulent diffusion. Furthermore, the models are calculated with radiative acceleration, which acts differently on different chemical species and can thus potentially explain

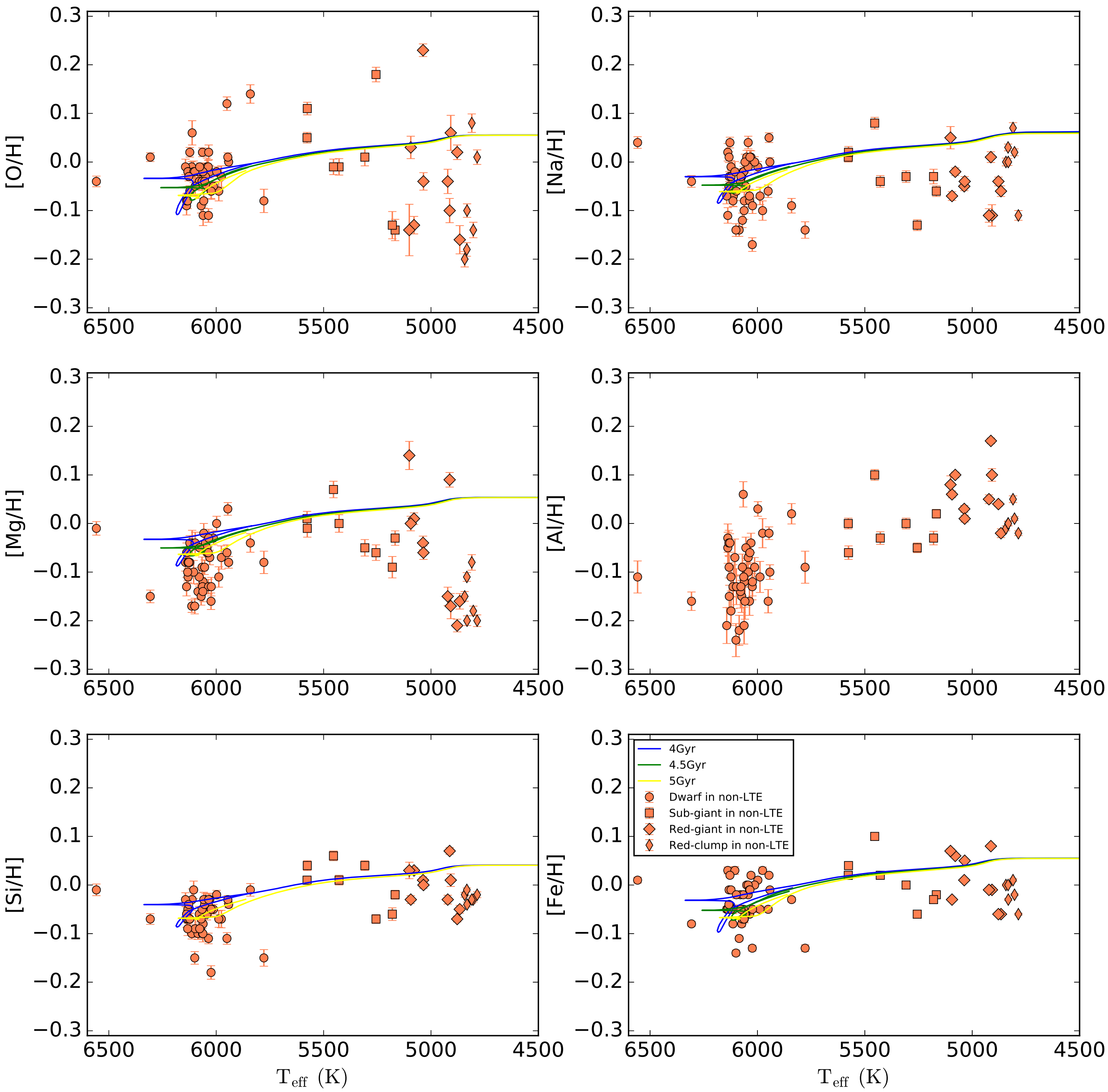

Figure 10. Non-LTE Abundances [X/H] as a function of effective temperature for individual M67 stars. We overplotted surface abundance isochrones from atomic diffusion models with solar metallicity and different evolution ages. Stars on different evolutionary state are marked as different symbols.

different abundance trends for the different elements under consideration.

In Fig. 10, we overplot the stellar evolutionary models on our results for the surface abundances versus effective temperature. Since the zero-point of the models are not relevant here and we are more interested in the effect of atomic diffusion on abundance trends, therefore, offsets have been applied to all the model abundances so as to match the model abundances with the solar mass and age 4.5 Gyr to the solar value (i.e. [X/H] = 0). In Table 3 we list all the offsets that have been added to the model abundances. Generally, our results broadly follow the trends predicted by the atomic diffusion models. The surface abundance depletion is most severe at the turnoff; the severity of this depletion is age-dependent, being more severe for older stars. Moving to later evolutionary stages (or lower effective temperature), the elements are brought back up to the surface by convective mixing (i.e. the first dredge-up), and so the surface abundance depletion becomes less severe; in giants, the models even predict a slight increase in the surface abundances over the initial values as a result of hydrogen being consumed during central H-burning. For O and Na, the models show the largest difference between the giants and dwarfs. This is caused by the little efficiency of radiative acceleration that these elements experience below the surface convection zone. On the contrary, the other species are expected to experience a larger radiative acceleration, especially for heavy element Fe. This reduces the effect of gravitational settling, resulting in a smaller difference between the surface abundances of dwarf and giant stars as compared to O and Na.

5.3 3D non-LTE effects

While the abundance trends we find in M67 are overall consistent with the predicted influence of atomic diffusion, we cannot exclude that our results are biased by deficits in the analysis. For example, to increase the accuracy of our abundance measurements further, 3D hydrodynamical model atmospheres should be considered. Such modelling is important for late type atmospheres, where the spectral line form at the top of the convective region, and eliminates the need for the artificial broadening parameters, such as microturbulence and macroturbulence. (e.g. Asplund et al. 2000).

Performing a 3D non-LTE study is beyond the scope of the present work. We note however that 3D corrections for the same lines can go in opposite directions for dwarfs and giants (e.g. Magic et al. 2013, Fig. 7). Consequently, it is possible that a 3D non-LTE analysis would find significantly flatter abundance trends than those presented in Sect. 4.3.

6 CONCLUSION

We have presented a comprehensive determination of the M67 elemental abundances of lithium, oxygen, sodium, magnesium, aluminium, silicon, and iron. We analysed lines using non-LTE and LTE calculations with 1D hydrostatic MARCS model atmospheres based on high resolution, high quality spectra from the GALAH survey.

We have accounted for non-LTE effects in the line formation of different elements. For lithium, non-LTE effects are not prominent. However, the large scatter in lithium abundances in stars with similar stellar parameters (i.e. mass, metallicity and age) may indicate the stars in this cluster could have different initial angular momentums to cause the different lithium depletions. In addition, we found a lithium-rich subgiant in our sample, which we confirmed to be a spectroscopic binary. It could be a potential candidate to study unusual lithium induced by tidal effect.

We found that star-to-star abundance scatter is reduced under non-LTE, compared to under LTE. Also, non-LTE analyses flattens the trends in surface abundances with effective temperature. However, abundance differences between stars in different evolutionary phases are not fully erased by non-LTE effects.

We compared our observed abundance trends with the trends predicted by the atomic diffusion model of Dotter et al. (2017), assuming solar metallicity and approximately solar age. Our non-LTE results and the models are broadly in agreement.

Finally, we underline the necessity to include accurate non-LTE corrections in order to obtain more reliable abundances to study abundance evolution and chemical tagging. Our analysis shows that, due to the potential influence of both systematic abundance errors and of stellar evolution effects, the method of connecting stars in the field to a common birth location by chemical similarity is significantly more reliable for stars in the same evolutionary phase, especially for subgiants.

ACKNOWLEDGEMENTS

XDG, KL, and AMA acknowledge funds from the Alexander von Humboldt Foundation in the framework of the Sofja Kovalevskaja Award endowed by the Federal Ministry of Education and Research, and KL also acknowledges funds from the Swedish Research Council (grant 2015-004153) and Marie Skłodowska Curie Actions (cofund project INCA 600398). This research has made use of the SIMBAD database, operated at CDS, Strasbourg, France.

REFERENCES

Amarsi A. M., Asplund M., 2017, MNRAS, 464, 264
Amarsi A. M., Asplund M., Collet R., Leenaarts J., 2015, MNRAS, 454, L11
Amarsi A. M., Asplund M., Collet R., Leenaarts J., 2016a, MNRAS, 455, 3735
Amarsi A. M., Lind K., Asplund M., Barklem P. S., Collet R., 2016b, MNRAS, 463, 1518
Asplund M., 2005, ARA&A, 43, 481
Asplund M., Nordlund Å., Trampedach R., Allende Prieto C., Stein R. F., 2000, A&A, 359, 729
Asplund M., Grevesse N., Sauval A. J., Scott P., 2009, ARA&A, 47, 481
Balachandran S., 1995, ApJ, 446, 203
Barklem P. S., 2016a, A&A Rev., 24, 9
Barklem P. S., 2016b, Phys. Rev. A, 93, 042705
Bautista M. A., 1997, A&AS, 122, 167
Bergemann M., Collet R., Amarsi A. M., Kovalev M., Ruchti G., Magic Z., 2017, ApJ, 847, 15
Berrington K. A., Burke P. G., Chang J. J., Chivers A. T., Robb W. D., Taylor K. T., 1974, Computer Physics Communications, 8, 149
Bertelli Motta C., Salaris M., Pasquali A., Grebel E. K., 2017, MNRAS, 466, 2161
Brault J., Neckel H., 1987, Tape copy from KIS IDL library
Bressan A., Marigo P., Girardi L., Salasnich B., Dal Cero C., Rubele S., Nanni A., 2012, MNRAS, 427, 127
Burke P. G., Hibbert A., Robb W. D., 1971, Journal of Physics B Atomic Molecular Physics, 4, 153
Canto Martins B. L., Lèbre A., de Laverny P., Melo C. H. F., Do Nascimento Jr. J. D., Richard O., de Medeiros J. R., 2006, A&A, 451, 993
Chen Y., Girardi L., Bressan A., Marigo P., Barbieri M., Kong X., 2014, MNRAS, 444, 2525
Choi J., Dotter A., Conroy C., Cantiello M., Paxton B., Johnson B. D., 2016, ApJ, 823, 102
De Silva G. M., Sneden C., Paulson D. B., Asplund M., Bland-Hawthorn J., Bessell M. S., Freeman K. C., 2006, AJ, 131, 455
De Silva G. M., Freeman K. C., Asplund M., Bland-Hawthorn J., Bessell M. S., Collet R., 2007, AJ, 133, 1161
De Silva G. M., et al., 2015, MNRAS, 449, 2604
Dotter A., 2016, ApJS, 222, 8
Dotter A., Conroy C., Cargile P., Asplund M., 2017, ApJ, 840, 99
Duong L., et al., 2018, preprint, (arXiv:1801.01514)
Freeman K., Bland-Hawthorn J., 2002, ARA&A, 40, 487
Friel E. D., Jacobson H. R., Pilachowski C. A., 2010, AJ, 139, 1942
García Pérez A. E., Asplund M., Primas F., Nissen P. E., Gustafsson B., 2006, A&A, 451, 621
Geller A. M., Latham D. W., Mathieu R. D., 2015, AJ, 150, 97
Gilmore G., et al., 2012, The Messenger, 147, 25
Gray D. F., 2005, The Observation and Analysis of Stellar Photospheres
Grevesse N., Asplund M., Sauval A. J., 2007, Space Sci. Rev., 130, 105
Gruyters P., Nordlander T., Korn A. J., 2014, A&A, 567, A72
Gruyters P., et al., 2016, A&A, 589, A61
Gustafsson B., Edvardsson B., Eriksson K., Jørgensen U. G., Nordlund Å., Plez B., 2008, A&A, 486, 951
Hobbs L. M., Thorburn J. A., 1991, AJ, 102, 1070
Holtzman J. A., et al., 2015, AJ, 150, 148

Kiselman D., 1993, A&A, 275
Korn A. J., Grundahl F., Richard O., Mashonkina L., Barklem P. S., Collet R., Gustafsson B., Piskunov N., 2007, ApJ, 671, 402
Kos J., et al., 2017, MNRAS, 464, 1259
Kos J., et al., 2018, MNRAS, 473, 4612
Kunder A., et al., 2017, AJ, 153, 75
Kurucz R. L., 1995, in Adelman S. J., Wiese W. L., eds, Astronomical Society of the Pacific Conference Series Vol. 78, Astrophysical Applications of Powerful New Databases. p. 205
Lambert D. L., 1993, Physica Scripta Volume T, 47, 186
Lind K., Asplund M., Barklem P. S., 2009a, A&A, 503, 541
Lind K., Primas F., Charbonnel C., Grundahl F., Asplund M., 2009b, A&A, 503, 545
Lind K., Asplund M., Barklem P. S., Belyaev A. K., 2011, A&A, 528, A103
Lind K., et al., 2017, MNRAS, 468, 4311
MacLean B. T., De Silva G. M., Lattanzio J., 2015, MNRAS, 446, 3556
Magic Z., Collet R., Hayek W., Asplund M., 2013, A&A, 560, A8
Magrini L., et al., 2014, A&A, 563, A44
Majewski S. R., et al., 2017, AJ, 154, 94
Martell S. L., et al., 2017, MNRAS, 465, 3203
Martin A. J., Stift M. J., Fossati L., Bagnulo S., Scalia C., Leone F., Smalley B., 2017, MNRAS, 466, 613
Mathieu R. D., Latham D. W., Griffin R. F., 1990, AJ, 100, 1859
Michaud G., Fontaine G., Beaudet G., 1984, ApJ, 282, 206
Nordlander T., Lind K., 2017, preprint, (arXiv:1708.01949)
Nordlander T., Korn A. J., Richard O., Lind K., 2012, ApJ, 753, 48
Önehag A., Korn A., Gustafsson B., Stempels E., Vandenberg D. A., 2011, A&A, 528, A85
Önehag A., Gustafsson B., Korn A., 2014, A&A, 562, A102
Osorio Y., Barklem P. S., 2016, A&A, 586, A120
Osorio Y., Barklem P. S., Lind K., Belyaev A. K., Spielfiedel A., Guitou M., Feautrier N., 2015, A&A, 579, A53
Pace G., Pasquini L., François P., 2008, A&A, 489, 403
Pace G., Castro M., Meléndez J., Théado S., do Nascimento Jr. J.-D., 2012, A&A, 541, A150
Pancino E., Carrera R., Rossetti E., Gallart C., 2010, A&A, 511, A56
Pasquini L., Biazzo K., Bonifacio P., Randich S., Bedin L. R., 2008, A&A, 489, 677
Peach G., Saraph H. E., Seaton M. J., 1988, Journal of Physics B Atomic Molecular Physics, 21, 3669
Pichardo B., Moreno E., Allen C., Bedin L. R., Bellini A., Pasquini L., 2012, AJ, 143, 73
Pinsonneault M. H., 2010, in Charbonnel C., Tosi M., Primas F., Chiappini C., eds, IAU Symposium Vol. 268, Light Elements in the Universe. pp 375–380 (arXiv:1001.3864), doi:10.1017/S1743921310004497
Piskunov N., Valenti J. A., 2017, A&A, 597, A16
Prantzos N., Charbonnel C., 2006, A&A, 458, 135
Randich S., Sestito P., Primas F., Pallavicini R., Pasquini L., 2006, A&A, 450, 557
Reader J., Kramida A., Ralchenko Y., 2012, in American Astronomical Society Meeting Abstracts #219. p. 443.01
Sanders W. L., 1977, A&AS, 27, 89
Sarajedini A., Dotter A., Kirkpatrick A., 2009, ApJ, 698, 1872
Schuler S. C., King J. R., The L.-S., 2009, ApJ, 701, 837
Scott P., et al., 2015, A&A, 573, A25
Sharma S., et al., 2017, preprint, (arXiv:1707.05753)
Sheinis A., et al., 2015, Journal of Astronomical Telescopes, Instruments, and Systems, 1, 035002
Skrutskie M. F., et al., 2006, AJ, 131, 1163
Smiljanic R., et al., 2016, A&A, 589, A115
Steenbock W., Holweger H., 1984, A&A, 130, 319
Takeda Y., 2003, A&A, 402, 343
Tang J., Bressan A., Rosenfield P., Slemer A., Marigo P., Girardi L., Bianchi L., 2014, MNRAS, 445, 4287
Tautvaišiene G., Edvardsson B., Tuominen I., Ilyin I., 2000, A&A, 360, 499
Turcotte S., Richer J., Michaud G., Iglesias C. A., Rogers F. J., 1998, ApJ, 504, 539
Villanova S., Carraro G., Saviane I., 2009, A&A, 504, 845
Wenger M., et al., 2000, A&AS, 143, 9
Wittenmyer R. A., et al., 2017, preprint, (arXiv:1712.06774)
Yadav R. K. S., et al., 2008, A&A, 484, 609
Yakut K., et al., 2009, A&A, 503, 165
Yong D., Carney B. W., Teixera de Almeida M. L., 2005, AJ, 130, 597
de Jong R. S., et al., 2012, in Ground-based and Airborne Instrumentation for Astronomy IV. p. 84460T (arXiv:1206.6885), doi:10.1117/12.926239
van Regemorter H., 1962, ApJ, 136, 906